



HAL
open science

Structural and functional modifications induced by X-ray nanopatterning in Bi-2212 single crystals

Valentina Bonino, Angelo Agostino, Carmelo Prestipino, Olivier Hernandez,
Matteo Fretto, Lorenzo Mino, Marco Truccato

► **To cite this version:**

Valentina Bonino, Angelo Agostino, Carmelo Prestipino, Olivier Hernandez, Matteo Fretto, et al..
Structural and functional modifications induced by X-ray nanopatterning in Bi-2212 single crystals.
CrystEngComm, 2018, 20 (42), pp.6667-6676. 10.1039/c8ce01183d . hal-01935363

HAL Id: hal-01935363

<https://univ-rennes.hal.science/hal-01935363>

Submitted on 7 Dec 2018

HAL is a multi-disciplinary open access archive for the deposit and dissemination of scientific research documents, whether they are published or not. The documents may come from teaching and research institutions in France or abroad, or from public or private research centers.

L'archive ouverte pluridisciplinaire **HAL**, est destinée au dépôt et à la diffusion de documents scientifiques de niveau recherche, publiés ou non, émanant des établissements d'enseignement et de recherche français ou étrangers, des laboratoires publics ou privés.

Structural and functional modifications induced by X-ray nanopatterning in Bi-2212 single crystals

Valentina Bonino¹, Angelo Agostino², Carmelo Prestipino³, Olivier Hernandez³, Matteo Fretto⁴, Lorenzo Mino², Marco Truccato¹

¹Department of Physics, Interdepartmental Centre NIS, University of Torino, via P. Giuria 1, I-10125 Torino, Italy

²Department of Chemistry, Interdepartmental Centre NIS and INSTM Centro di Riferimento, University of Torino, via P. Giuria 7, I-10125 Torino, Italy

³ University of Rennes, CNRS, ISCR (Institut des Sciences Chimiques de Rennes) - UMR 6226, F-35000 Rennes, France.

⁴Nanofacility Piemonte INRiM (Istituto Nazionale di Ricerca Metrologica), Strada delle Cacce 91, 10135, Torino, Italy

Abstract

We have investigated the modifications induced in the high- T_c superconductor $\text{Bi}_2\text{Sr}_2\text{CaCu}_2\text{O}_{8+\delta}$ (Bi-2212) by X-ray nanopatterning, which is an innovative, photoresist-free, direct-writing approach recently used to fabricate proof-of-concept electrical devices [Truccato et al., Nano Lett. 2016, 16, 1669]. By means of combined synchrotron microdiffraction and electrical transport measurements carried out on the same Bi-2212 microcrystal, we show that hard X-ray irradiation with fluences of the order of 10^{12} J/m^2 , corresponding to doses of the order of 10^{13} Gy , induces crystal fragmentation into multiple subdomains and decreases the carrier density of the system. We ascertain that the synergistic action of grain boundaries and of oxygen removal from the material dramatically changes the properties of Bi-2212 both in the normal and in the superconducting state. This special feature of X-ray nanopatterning introduces an opportunity that could be exploited to finely tune material structural defects according to the desired properties.

Keywords: synchrotron, nanobeam, direct-write patterning, high-temperature superconductors, Bi-2212, oxygen, grain boundary, X-ray nanopatterning

Introduction

Lithographic methods lie at the heart of modern-day nanotechnology. Their development in the reduction of pattern motif in functional materials has enabled the fabrication of high-performing and cost-effective integrated circuits, storage devices, displays, biosensors, DNA microarrays and advanced materials ¹. The main improvements in the past few decades were mainly based on the decrease of the radiation wavelength, which has enabled a corresponding decrease of the minimum feature size, so that nowadays 193 nm ArF lasers represent the standard for high volume production. However, further decrease towards shorter wavelengths at the moment is limited only to research and development activities, mainly due to the lack of suitable laser sources or photoresists compliant with industrial standards. For instance, this is still the case for Extreme UltraViolet (EUV) lithography exploiting $\lambda = 13.5$ nm, which is considered a good candidate for the sub-20 nm technological nodes and indeed has already shown the capability to produce patterns with resolutions down to 8 nm half-pitch in its interference version ².

A very different approach could be represented by the use of intense, highly-focused, hard X-ray beams to tailor the material growth and properties at the nanoscale. Indeed, X-rays produced by synchrotrons and free electron lasers have already proved to be able to stimulate the organized growth of nanostructures ³, to manipulate defects ⁴ and to modify the properties of materials ⁵. From this point of view, the viability of an approach based on maskless X-ray nanopatterning has been recently demonstrated by Truccato *et al.* by fabricating a proof-of-concept electrical device out of the superconducting oxide $\text{Bi}_2\text{Sr}_2\text{CaCu}_2\text{O}_{8+\delta}$ (Bi-2212) ⁶. This patterning method represents a conceptual novelty because it does not imply any material removal from the substrate and is just based on the spatial modulation of the lattice electrical properties, with great potential advantages in terms of heat dissipation, chemical contamination and mechanical stability of the devices.

However, the full development of this patterning technique requires a good understanding of the underlying chemical-physical mechanisms that connect the X-ray exposure with the changes in the electric properties, in order to finely tune the desired modifications. The processes involved are expected to depend on the material absorption properties and on dis-excitation mechanisms, that in turns depend on the material composition and structure, the X-ray wavelength, irradiation dose and possibly from the X-ray flux and exposure time. Indeed, several mechanisms have been evoked so far in literature for material modifications induced by X-rays, including for instance sample heating, formation of electronic defects or excited states, photoreduction of metallic ions due to photoelectron generation, production of highly reactive species from solutions as a consequence of radiolysis, and modifications of the liquid surface tension due to surface charge accumulation⁷. On the other hand,

in the specific case of Bi-2212, the creation of oxygen vacancies and the increase of crystallographic mosaicity have been considered as possibly responsible for the increase of the superconducting critical temperature after irradiation ⁶.

However, a detailed study of these modifications has not been performed yet, to the best of our knowledge. The present paper is devoted to fill this gap by studying the effect of successive X-ray exposures on Bi-2212 in order to obtain more insight on the structural phenomena underlying X-ray nanopatterning.

Experimental

The experimental strategy we have followed consists in repetitively exposing high-quality Bi-2212 microcrystals to X-rays, and in monitoring step by step the corresponding effects on their crystal structure by means of X-ray micro-diffraction, whereas changes in the superconducting and normal state properties have been monitored by means of electrical measurements. Due to time and experimental constraints at the synchrotron, a parallel sample strategy has been adopted where the samples have been produced with very similar initial features and underwent the same irradiation procedure. However, only one specifically prepared sample also underwent electrical measurements, which required the X-ray diffraction acquisition procedure to be adapted to its special features.

Sample preparation. A set of straight whisker-like Bi-2212 microcrystals showing mirror surfaces and regular shapes has been selected under an optical microscope (100× magnification) from a batch produced following the procedure described elsewhere ⁸. From this set two similar whisker crystals have been selected, the first one was used to study the irradiation effect in the absence of any physical constrain (the so-called freestanding crystal, i.e. with just one of its extremities fixed on a glass rod by glue), while the second one was integrated in an electric chip. More precisely, the second whisker was mounted onto a sapphire substrate with its *c*-axis normal to the substrate plane and then four electrical contacts have been fabricated via Ag physical vapour deposition. A picture of this sample is shown in Figure 1.

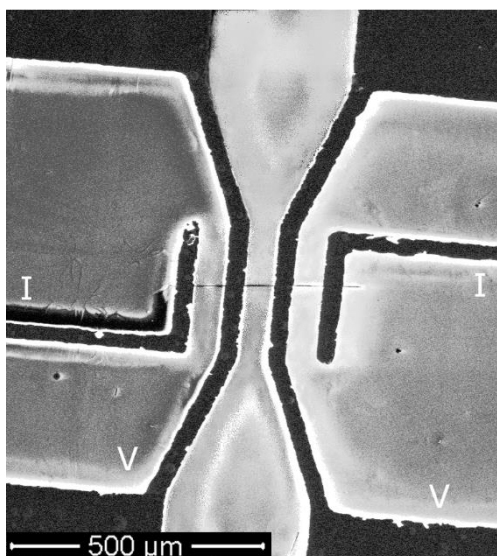


Figure 1: Micrograph of the mounted-on-chip sample (WBLP04). The Bi-2212 crystal is the thin horizontal line at the centre of the image. The four Ag strips vertically crossing the crystal represent the electrical contacts and are labelled according to their connection to the measurement circuit.

The so-obtained chip has undergone an annealing at 450°C for 5 minutes (heating and cooling rates equal to 5 K/min) in 1 bar pure oxygen atmosphere in order to secure good electrical contacts minimizing possible changes in the crystal oxygen content. Indeed, the total oxygen diffusion length in the ab -plane during this thermal cycle is $1.7 \mu\text{m}$ ⁹, which in principle could induce some variations in the oxygen content, but the fact that superconducting critical temperature T_c for this crystal in pristine conditions is $T_c = 78.3 \text{ K}$ testifies that these changes, if any, are small enough to keep the crystal in its native overdoping regime^{10, 11} (see the following for more details). Finally, in order to create a reference point for the irradiation procedure, two Pt pillars about $1 \mu\text{m}$ high were deposited on the sapphire substrate in close proximity of the crystal by Focused Ion Beam (FIB)-assisted vapor deposition (FEI QuantaTM 3D FIB, with Ga-ion current of 10 pA). Scanning electron microscope (SEM) analysis has determined the sizes of the region of this crystal between the voltage contacts as $168.7 \times 4.69 \times 0.33 \mu\text{m}^3$ (along the a -, b -, and c -axis directions, respectively), whereas the thickness of Ag contacts is about $2.1 \mu\text{m}$. Figure S1 of the Supplementary Information displays the appearance of the central region of the sample at the end of the preparation procedures.

Electrical measurements. The sample was electrically characterized along its ab crystallographic plane by the standard four-probe method. Measurements of the electrical resistance R were performed in a continuous flow Janis ST-100 helium cryostat in the temperature range $40 \text{ K} \leq T \leq 290 \text{ K}$. The R

vs T behaviors were acquired on warming by means of temperature ramps at the constant rate of 0.5 K/min and with a current value of 1 μ A. The sample was stabilized at low temperature for at least one hour before every measurement. The substrate was accurately cleaned from any residuals and a thin layer of cryogenic high vacuum grease was applied to provide good thermal contact to the sample holder. T_c has been calculated as the inflection point of the R vs T curves, however, in order to analyze the presence of secondary superconducting phases, also a zero-resistance superconducting temperature T_{c0} has been defined as the first non-zero resistance point above noise level.

X-ray set-up. The X-ray irradiation and characterization was performed at the microdiffraction ID13 beamline at the European Synchrotron Radiation Facility (ESRF) in Grenoble, France. The microbeam generated by an 18 mm period in-vacuum undulator was monochromatised to $E_0 = 13.0$ keV and focused to a spotsize $S_b = 2 \times 2.5 \mu\text{m}^2$ (horizontal \times vertical). The beam flux Φ_0 was estimated in 4×10^{11} ph/s and fully used for crystal irradiation, whereas during the characterization the flux has been lowered by 2 orders of magnitude by an opportune absorber in order to prevent further significant exposure. The experimental station was equipped with a Frelon CCD camera¹² placed about 50 mm away from the sample. Tilt and distance of the camera were aligned using a LaB₆ standard in a rotating capillary, finer adjustment has been done during data analysis.

The chip and the freestanding whisker-like crystal were alternately mounted on a motor stage composed by a three dimensional piezo translation stage (x,y,z) installed over a rotation stage (φ) with the rotation axis perpendicular to the storage ring plane, and intersecting the beam in the focus point, with the crystallographic a -axis indicatively parallel to the φ -axis. However, due to the sphere of confusion of the setup, the small size of the whisker and the limited allowed range of rotation for the mounted crystal, the alignment of the center of rotation, the whisker and the beam was not precise enough to keep the beam on the crystal along all the precession. For this reason, a horizontal translation motor perpendicular to the beam was scanned during irradiation or diffraction measurements with a step equal to the half width half maximum (HWHM) of the beam over a range greater than the alignment error estimated during sample alignment. This approach has allowed to deliver a constant energy profile to the crystal during the irradiation and to obtain the most significant sampling during diffraction.

Diffraction patterns have been acquired as a function of φ position every 0.2° . Due to the fact that the sapphire substrate is not transparent to the X-rays, the diffraction acquisition of the mounted-on-chip sample was limited to a φ range of 20° from the position with the b axis aligned with the beam, whereas the freestanding sample has been investigated over the maximum allowed range of 270° .

The region of interest of the mounted-on-chip sample was located by taking as a reference the diffraction of the two Pt pillars.

X-ray data treatment. As previously mentioned, for each angular position φ a set of frames (from 8 to 10, depending on sample alignment) has been collected, but due to the strong anisotropy and small sizes of the crystal along both the b - and the c -axis, only in one or two images the beam was actually on the sample. For this reason, a software has been developed to select the most significant frame for each angular position. For the freestanding sample the algorithm is very simple and selects for each set only the frame with the higher average pixel value, since when the sample is out of the beam only the small signal coming from air scattering is detected, whereas, when the sample is within the beam the signal generated by Bi-2212 is much stronger. For the mounted-on-chip sample the algorithm cannot use this scattering contrast anymore, because the average pixel intensity is dominated by the scattering of the substrate. In order to select the correct frames, we have taken advantage of the alignment of the BSCCO a -axis with the φ -axis: in this case all of the (00 l m) reflections fall in a small region along the detector equatorial axis, so that the average of the pixel values has been calculated in this region only. Moreover, in order to avoid selection errors induced by streaks due to strongly saturated substrate peaks, the translation position of the selected frames has been fitted by a polynomial and the outlier positions have been revised manually. The subset of images obtained in this way has been analysed either by the CrysAlis software made available from Rigaku or subjected to an image treatment software developed *ad hoc*. The latter software allows performing pixel-wise maximum projections over a set of data (implementing a maximum intensity filter to reduce the contribution to the images stemming from saturating substrate reflections), and mosaic figures showing a small range of the detector along the φ rotation.

The evaluation of the c -axis length has been performed over the radially integrated average image by using the Le Bail fit algorithm¹³ implemented on the FullProf code¹⁴. Radial integration has been performed with the help of the Fit2D code¹⁵ with calibration parameters refined from LaB₆ and corundum standards. Before integration, the averaged images were totally masked, with the exception of a stripe corresponding to the (00 l m) reflections. This preliminary operation was mandatory in order to avoid the interference from the substrate reflections that are several orders of magnitude higher. It is worth noticing that the fits used to calibrate the Frelon camera were highly unstable due to the spottiness of the images collected for the standards, for this reason the sample-detector distance has been recalibrated by about 2% in order to obtain the expected value of the c -axis for the pristine sample.

Irradiation sessions and XRD analysis

The aim of the present paper is to monitor the changes induced in Bi-2212 by multiple and prolonged X-ray irradiation sessions via both scanning X-ray diffraction and electrical measurements. The irradiation procedure was performed by scanning during each session the same region, which was placed 20 μm above the Pt reference and extended over 7.5 μm along the a -axis and over the whole crystal thickness (0.33 μm) along the c -axis. The experiment followed a multistage procedure, performing in-series: i) a preliminary μ -XRD analysis, ii) an irradiation session, iii) a post-irradiation μ -XRD analysis, and iv) an off-line electrical characterization, and then repeating the sequence. The electrical measurement was carried out only for the mounted-on-chip sample. In order to assess the optimum irradiation time per point, the first irradiation session was performed in three stages of 480 s per point, at the end of which the first electrical measurement was performed. Subsequently, all of the three successive irradiations were carried out using 1440 s per point.

| Irradiation # | Δt (s/point) | F (10^{11}J/m^2) | CF (10^{11}J/m^2) | D (10^{12}Gy) | CD (10^{12}Gy) | |
|---------------|----------------------|-------------------------------|--------------------------------|----------------------------|-----------------------------|-------|
| 1 | .a | 480 | 2.559 | 2.559 | 1.303 | 1.303 |
| | .b | 480 | 2.559 | 5.118 | 1.303 | 2.606 |
| | .c | 480 | 2.559 | 7.677 | 1.303 | 3.909 |
| 2 | 1440 | 7.677 | 15.354 | 3.907 | 7.816 | |
| 3 | 1440 | 7.677 | 23.031 | 3.907 | 11.723 | |
| 4 | 1440 | 7.677 | 30.708 | 3.907 | 15.630 | |

Table 1: Irradiation time Δt per point of the rastered mesh, fluence F , cumulative fluence CF delivered to the exposed surface, dose D and cumulative dose CD estimated for the irradiated volume of the Bi-2212 samples.

Table 1 reports the irradiation details with the delivered fluence F and the absorbed dose D for each single irradiation, along with the corresponding cumulative values. The absorbed dose D is calculated from the Beer–Lambert law as:

$$D = \frac{\Phi_0 \Delta t E_0 \eta}{m_\phi} = \frac{\Phi_0 \Delta t E_0 \left(1 - e^{-\frac{t}{\lambda_a}}\right)}{V_\phi \rho},$$

where the Δt is the irradiation time per point and m_ϕ the mass of the irradiated volume, which corresponds to the product between the crystal density ρ and the sample volume V_ϕ struck by the beam. The factor $\eta = 1 - \exp(-t/\lambda_a)$ takes into account the decaying absorption of the incident radiation

within a crystal with length t and attenuation length λ_a . Given $E_0 = 13.0$ keV, λ_a for Bi-2212 is equal to $26.91 \mu\text{m}^{16}$.

Results and discussion

$\text{Bi}_2\text{Sr}_2\text{CaCu}_2\text{O}_{8+\delta}$ was discovered as a high- T_c superconductor by Maeda *et al.*¹⁷ and features a complex, incommensurably modulated, layered structure composed of perovskite and rock salt sub-units with superspace group $Bbmb$ ($0\beta 1$) and a pseudo-tetragonal cell ($a \approx b \approx 5.4 \text{ \AA}$, $c \approx 30.7 \text{ \AA}$) with modulation vector $q^*=[0, 0.210, 1]$. Its transport properties are strongly dependent on the non-stoichiometric oxygen content δ , which refers to the amount of oxygen atoms hosted in the interstitial sites between the BiO and SrO layers and determines the amount of hole-doping of the material. Indeed, it is well-known that δ modulates the normal state electrical resistivity ρ (i.e. ρ decreases with increasing δ) and also affects T_c , even if in a non-monotonic way, because a single δ value exists corresponding to the highest T_c (the so-called optimal doping regime, OP), with lower T_c values corresponding both to lower δ values (the so-called underdoped regime, UD) and to higher δ values (the so-called overdoped regime, OD). Moreover, δ directly affects also the c -axis length, with higher δ values corresponding to shorter c -axis lengths.

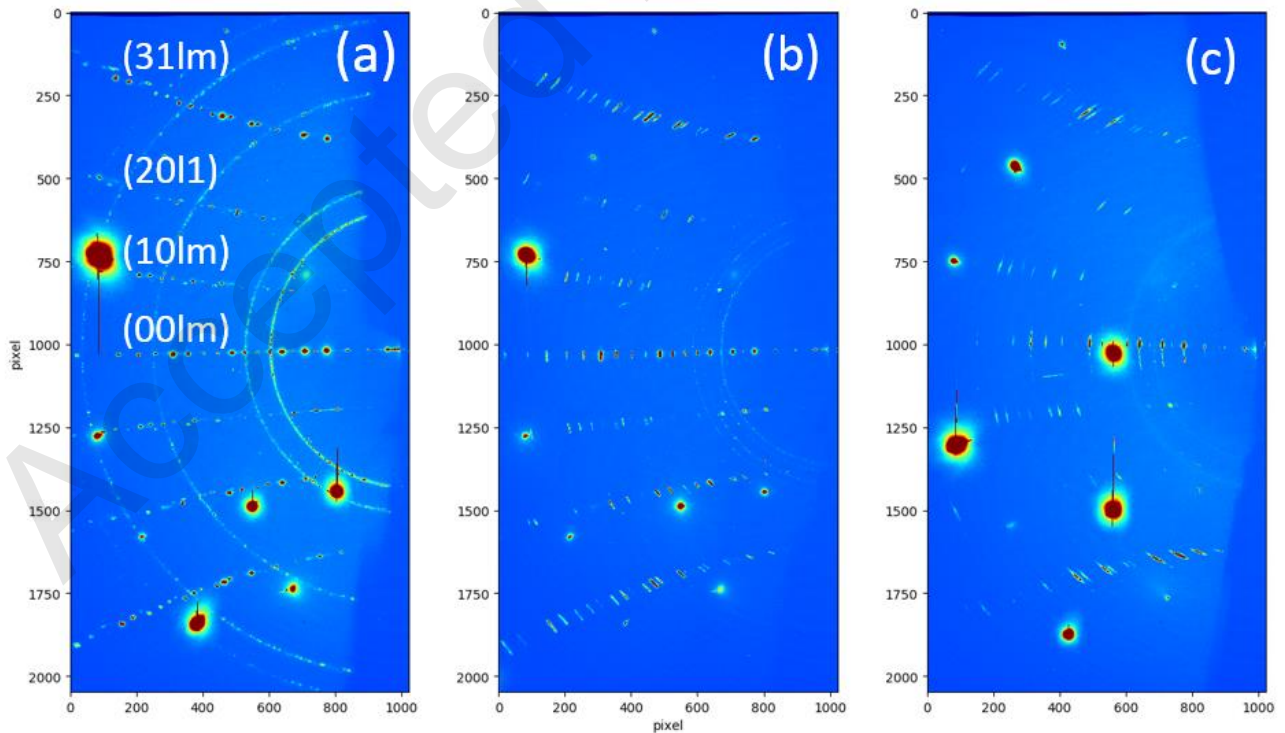


Figure 2: Maximum projection maps of the micro-diffraction patterns collected during a 20° scanning around the a -axis (ϕ -axis). The panels refer to the following irradiation conditions of the sample: pristine

(a), after a cumulative dose $CD=3.909 \times 10^{12}$ Gy and cumulative fluence $CF=7.677 \times 10^{11}$ J/m² (b), and after a cumulative dose $CD=15.630 \times 10^{12}$ Gy and a cumulative fluence $CF=30.708 \times 10^{11}$ J/m² (c). Indexing of the reflections is reported in panel (a).

Figure 2 shows the maximum projections of a 20° φ -scan of the contacted whisker, with the a -axis aligned along the rotation axis itself in the vertical direction. This figure compares the sample in the pristine state (a), after a cumulative fluence $CF=7.677 \times 10^{11}$ J/m² (b), and after $CF=30.708 \times 10^{11}$ J/m² (c, see Table 1). Inspection of the pattern of the pristine state (Figure 2(a)) confirms that the sample remains crystalline after the electrical contact process, and that the frame is composed of three different features: i) a few isolated very strong peaks, due to reflections of the sapphire substrate, ii) four continuous rings ascribed to the (111), (200), (220), and (311) reflections of Ag used for contact deposition, that are present only at lower angles, and finally iii) seven rows of peaks that can be ascribed to BSSCO reflections. In agreement with our experimental setup in which the exploration of the reciprocal space is strongly limited by the Ewald sphere curvature and by a rotation limit of 20°, the series of peaks can be identified with the (00 l m), (10 l m), (20 l 1), and (31 l m) reflection series of Bi-2212, from the equatorial axis of the detector to the top, and with the corresponding series featuring opposite values for the h index in the lower part of the detector, with a small intensity asymmetry between the two regions of the detector due to the misalignment between the a and φ axes. It is possible to notice that the Ag contribution disappears after the irradiation cycles, probably because of the interaction between the Ag particles and the beam. Also a few changes in the substrate reflections are visible, probably due to a different alignment between the sapphire substrate and the crystal, which could have been originated from the thermal contractions and dilations induced by the cryogenic electrical measurements taken between the diffraction measurements; however, a non-constant efficiency of the algorithm used to reduce the contribution of the substrate reflections to the image cannot be excluded. From Figure 2 it is also visible that the main effect of the radiation damage is on the Bi-2212 crystal mosaicity: indeed, the sample remains a single crystal but the reflections that look like circular spots in the pristine sample decrease in intensity and assume an elongated shape with increasing the cumulated fluence.

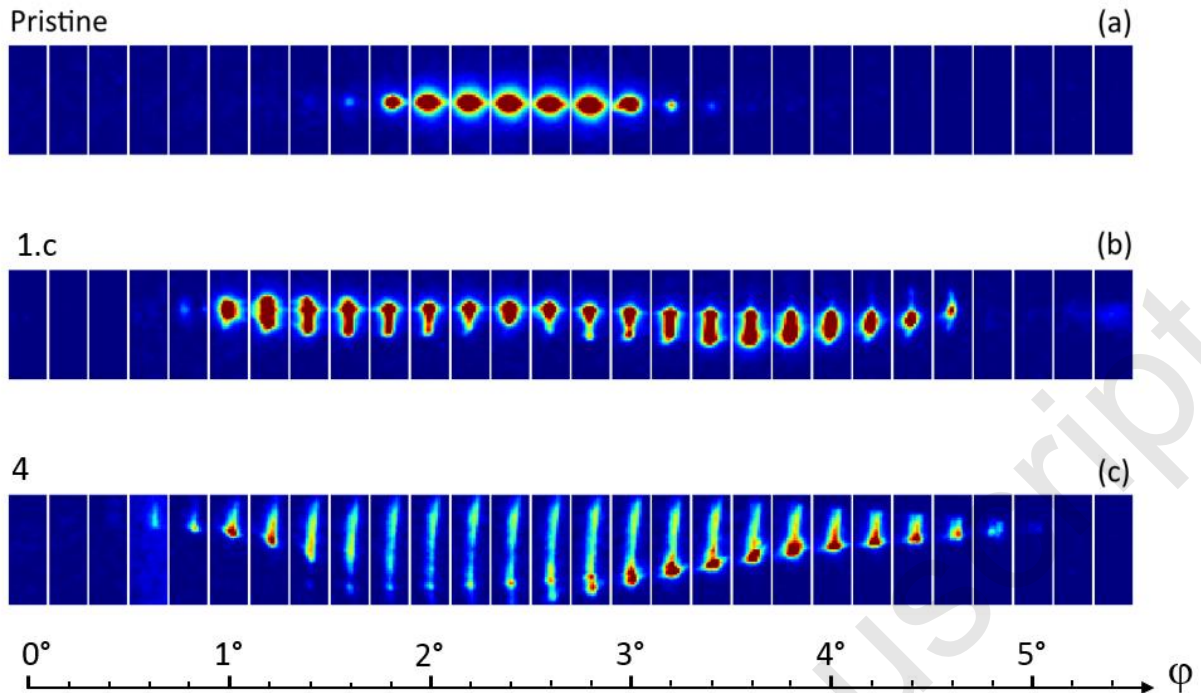


Figure 3: Mosaic image of the (0 0 14) reflection as a function of the ϕ rotation in steps of 0.2° , selected from the maximum projections of Figure 2. Panel (a) corresponds to the pristine sample, panel (b) to cumulative dose $CD=3.909 \times 10^{12}$ Gy and cumulative fluence $CF=7.677 \times 10^{11}$ J/m² (irradiation #1.c) and panel (c) to $CD=15.630 \times 10^{12}$ Gy and $CF=30.708 \times 10^{11}$ J/m² (irradiation #4, see Table 1).

More detailed information can be obtained from Figure 3, which focuses on the (0 0 14) reflection and shows the evolution of the shape of the peak as a function of the fluence and of the ϕ position. In the pristine sample the peak can be considered as gaussian along the two directions of the detector axes and also along the ϕ rotation. Upon irradiation, the peak deforms irregularly in the vertical direction forming a small arc and spreads over a wider range in the ϕ rotation. The fact that the 2 θ direction is less affected and the irregular nature of the other deformations indicate that such behavior should be ascribed to an increase of the crystal mosaicity and not to an increase of internal strain of the whisker. Indeed, the deformation of the gaussian spots of the pristine material into arc-like features with increasing the cumulative fluence is compatible with the interpretation that the irradiated portion of the crystal is fragmented in multiple nano-domains slightly misaligned and connected to each other by [010]-tilted grain boundaries. Moreover, the increase of the amplitude of the ϕ range where the reflection can be observed from about 2° for the pristine material up to about 4.4° for $CF=30.708 \times 10^{11}$ J/m² seems to indicate that the irradiation also promotes the appearance of [100]-tilted grain boundaries. We cannot exclude that this fragmentation process could be somehow affected

also by individual features of the crystals, including for instance the release of some strain imposed to the whisker during the procedure of chip fabrication. Indeed, Figure 3(a) shows for the mounted-on-chip pristine sample a significant intensity of the (0 0 14) peak for about 2° during the φ -rotation, therefore revealing a more broadened rocking curve compared to the one of the free-standing sample, which, under the same instrumental conditions, shows the presence of this peak only in a single diffraction image, with a corresponding rocking curve width of about 0.2° during the φ -rotation.

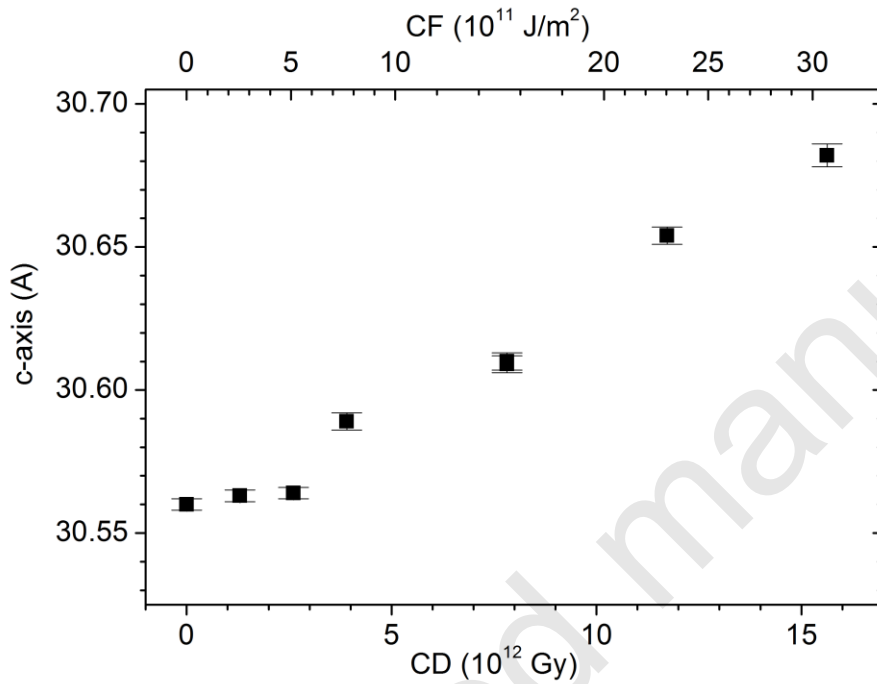


Figure 4: c-axis length versus cumulative dose CD and cumulative fluence CF for the mounted-on-chip crystal at different stages of the experiment.

| Pristine | Post Irradiation #1a | Post Irradiation #1b | Pre Irradiation # 2 | Post Irradiation # 2 | Pre Irradiation # 3 | Post Irradiation # 3 | Post Irradiation # 4 |
|------------|----------------------|----------------------|---------------------|----------------------|---------------------|----------------------|----------------------|
| 30.560 (2) | 30.563 (2) | 30.564 (2) | 30.589(3) | 30.61(3) | 30.609(3) | 30.654(3) | 30.682(4) |

Table 2: Values in Å of the c -axis as determined by the fit of the radially integrated intensity at different stages of the experiment.

The c -axis lattice parameters evaluated by Le Bail fit of the radially integrated intensities are listed in Table 2 and shown in Figure 4. The plots showing the integrated intensity and the quality of the fit are available in the Supplementary Information (see Figure S2 and Tables ST1 and ST2). It can be

noticed that the length of the c -axis increases with increasing the radiation fluence. This behavior confirms the general trend already observed in Bi-2212 by our group¹⁸, although the variation of the c -axis length shows some discrepancies with respect to our previous study. The key feature of the present experiment is represented by the acquisition of diffraction patterns via sample precession. This approach, compared to the previous nano-diffraction setup¹⁸, presents the advantage of allowing a more certain indexing of the pattern and to fully explore the spread of the reflections in the reciprocal space so that smaller uncertainties can be obtained and appearance of sub-domains can be detected. In any case, these data confirm that, under some circumstances, part of the radiation damage induced by X-ray nano-beams in Bi-2212 is compatible with the mechanism of oxygen depletion, as recently modelled by our group¹⁹.

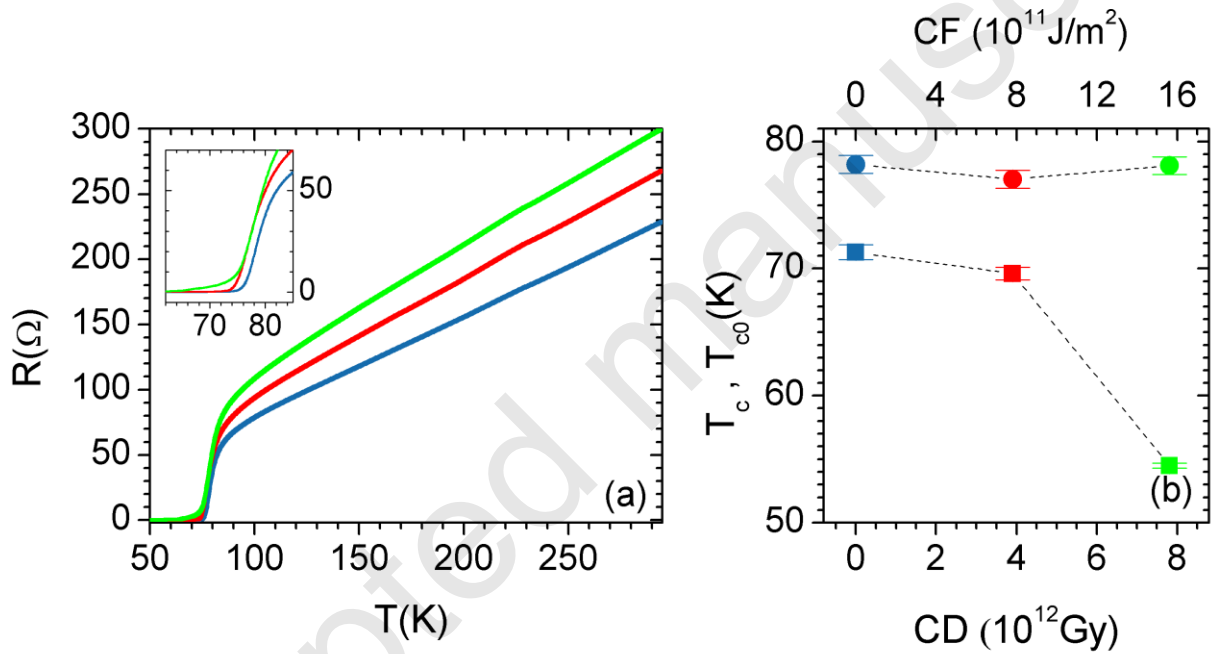


Figure 5. Panel (a): Four-probe R versus T behavior for the mounted-on-chip sample: before irradiation (blue), after a cumulative dose $CD=3.909 \times 10^{12}$ Gy and cumulative fluence $CF=7.677 \times 10^{11}$ J/m² (red), and after $CD=7.816 \times 10^{12}$ Gy and $CF=15.354 \times 10^{11}$ J/m² (green). The inset shows a magnification of the region around the superconducting transition. Panel (b): Critical temperature T_c (circles) and zero-resistance critical temperature T_{c0} (squares) versus cumulative dose CD and cumulative fluence CF .

The electrical resistance R of the mounted-on-chip sample is reported in Figure 5(a) as a function of temperature for the pristine condition, after a cumulative fluence $CF=7.677 \times 10^{11}$ J/m² (irradiation #1.c) and after $CF=15.354 \times 10^{11}$ J/m² (irradiation #2). A subsequent irradiation up to $CF=23.031 \times 10^{11}$ J/m² (irradiation #3) has induced a transition to an insulating state ($R > 20$ M Ω), preventing the measurement of the corresponding electrical behavior. A SEM inspection has revealed that after this

irradiation the crystal was still continuous, even if clearly deformed (see Fig. S3). These results provide valuable information about both the superconducting and the normal state.

Concerning the superconducting behavior, the corresponding transition is highlighted in the inset of Figure 5(a), where the appearance of a tail with increasing the cumulative fluence is visible. This phenomenon can be properly described by comparing the critical temperature T_c to the zero-resistance temperature T_{c0} . Their behavior as a function of both CF and CD is shown in Figure 5(b). It can be noticed that no clear variation can be observed for T_c beyond the experimental error. Considering that the irradiated and non-irradiated portions of the sample are electrically in series and that the corresponding lengths are $7.5 \mu\text{m}$ and $161.2 \mu\text{m}$, respectively, it is expected that the main contribution to the sample resistance comes from the non-irradiated part, unless the resistivity ρ of the irradiated part increases above a level about $161.2/7.5 \approx 21$ times greater than the pristine one. However, this is not the case for the curves of Figure 5(a), as it is discussed in more details in the following. Therefore, it is reasonable to associate the inflection point of the whole R vs T signal to the T_c of the non-irradiated part, which turns out to be practically constant, as expected. On the contrary, T_{c0} is clearly affected by the irradiation process and its difference from T_c increases with increasing the cumulative fluence, up to a maximum difference of about 24 K after a cumulative fluence $CF=15.354 \times 10^{11} \text{ J/m}^2$.

These modifications of the superconducting transition with increasing the irradiation dose are in agreement with the results obtained from previous studies, especially about the appearance of a tail even when only a portion of the sample with the shape of a trench is irradiated^{6, 18, 20}. This experimental observation is compatible with a picture where the $7.5 \mu\text{m}$ long irradiated portion actually consists of a large number of very short (e.g. 100-200 nm) crystal domains, each of them with different T_c , critical current density J_c and ρ values that are functions of the local cumulative damage of the crystal structure and of the kind of interconnection with the other crystallites. Indeed, if we assume that some interaction between different irradiation points has taken place from the point of view of the damage, which somehow extends beyond the HWHM limits of the beam¹⁹, a spatial distribution of T_c 's can be expected with the lowest values in the middle of the irradiated portion of the sample and increasingly higher values towards its boundaries. A similar behavior can also be expected for the local normal state resistivity $\rho(T)$, with higher values in the center of the irradiated region and decreasing values approaching the pristine one towards its limits. With increasing the temperature, each damaged crystal domain switches to the corresponding normal state curve $\rho(T)$, starting from the middle of the irradiated region and progressively adding its contribution to the sample resistance. However, each individual domain contribution to the sample resistance R is expected to be small, even if the local $\rho(T)$ values can be considerably greater than the pristine value,

because of the very short length of the domain. The superposition of all of these behaviors is expected to result in a slowly increasing R value of the sample as a function of T (i.e. the tail), until the T_c value of the large non-irradiated part is reached and a steep transition is observed.

Of course, this picture is in agreement with the indications coming from the diffraction measurements reported in Figure 3 about the progressive transformation of the single crystal towards a polycrystalline structure. From the point of view of the relationship between the changes of the crystal structure and the local values of T_c and $\rho(T)$, in principle the possible interpretation is twofold. On one hand, if different crystal domains appear, then grain boundaries originate as well. Their effect on the properties of high temperature superconductors has been extensively studied²¹, and it has been proved that they deeply affect transport properties, mainly depending on the magnitude of the misalignment angle between adjacent grains. As an example, in $\text{YBa}_2\text{Cu}_3\text{O}_{7-x}$ a steep decrease of the intergrain critical current was found for misorientation angles above 10° ²². Also in Bi-2212 Li Q. *et al.* proved that a 7° grain boundary was sufficient to suppress by about 9 K the T_c of a bicrystal film²³. A similar effect was also shown in Bi-2223 for grain boundaries misorientations of the order of 30° ²⁴. In all of these studies, the modifications of the transport properties have been associated to the introduction of local structural disorder at the grain boundaries, which induces the presence of local inhomogeneity. On the other hand, irradiation could directly affect the structure of the individual crystal nano-domains. Indeed, concerning for instance $\text{YBa}_2\text{Cu}_3\text{O}_{7-x}$, it has already been shown that electron irradiation can induce oxygen displacement and hole depletion²⁵. About Bi-2212, it has been proved that ion irradiation can directly modify the non-stoichiometric oxygen content δ , inducing an increase of the c -axis length up to about 0.4 \AA , corresponding to a transition from superconducting to insulating electrical behavior^{26, 27}. Moreover, oxygen removal from single crystals has also been induced by means of ordinary thermal annealing under controlled atmosphere: in the case of whisker-like Bi-2212 single crystals very similar to the ones used in the present experiment, a change in the c -axis length by about 0.15 \AA has been observed to correspond to a change in the doping status from OD to UD¹¹.

Actually, the data shown in Figure 3 and Figure 4 testify that both effects are present in our irradiated sample. Although each of them cannot individually explain the observed effects on the electrical behavior we have observed, they seem to act in a synergistic way to enhance each other. Indeed, the maximum crystal domain misalignment of about 4.4° that can be deduced from Figure 3(c) for $CF=30.708 \times 10^{11} \text{ J/m}^2$, if compared to previous results²²⁻²⁴ should not significantly affect T_c , which would imply a practically constant value of T_{c0} that is not confirmed by our measurements.

In the same way, an elongation of the c -axis length of about 0.09 \AA like the one observed for $CF=23.031 \times 10^{11} \text{ J/m}^2$ can be expected at most to result into a shift from the OD to the UD regime,

with T_c still in excess of 70 K¹¹, whereas in other cases it has resulted in a change of T_c by 5-7 K only²⁸. On the contrary, our measurements have shown that values of $CF \geq 23.031 \times 10^{11}$ J/m² have turned the material into an insulating state, which is not expected on the basis of each individual effect.

This synergistic action of crystal fragmentation and oxygen depletion represents the key result of the present experiment and introduces a more complex mechanism with respect to the picture emerging from our previous work on nano-diffraction¹⁵. This mechanism also clarifies why oxygen removal by photogenerated electrons is not able to explain by itself all of the experimental data available for Bi-2212¹⁹, suggesting that the influence of grain boundaries is expected to be larger for dense irradiation meshes. Moreover, this could also imply that much care has to be taken when comparing experimental results originated by thermodynamic equilibrium processes, like for instance thermal annealing, to experimental results originated by processes quite far from thermodynamic equilibrium, like for instance ion and X-ray irradiation.

Concerning the normal state resistivity ρ of Bi-2212 material, its behavior as a function of T is displayed in Figure 6(a) for the pristine sample and for two different levels of irradiation. It is worth noticing that the ρ values of the irradiated material have been calculated under the simplifying assumption that the irradiated portion of the crystal features uniform structural damage and corresponding uniformly changed electrical properties. Consequently, the sample has been schematized as an electrical resistance representing the irradiated portion of the crystal (whose uniform resistivity is a function of irradiation) that is electrically in series with the remaining pristine part. The corresponding mathematical model allows for the determination of $\rho(T)$ for each irradiation level, apart from the region very close to T_c where some artifacts appear and that has not been reported for this reason.

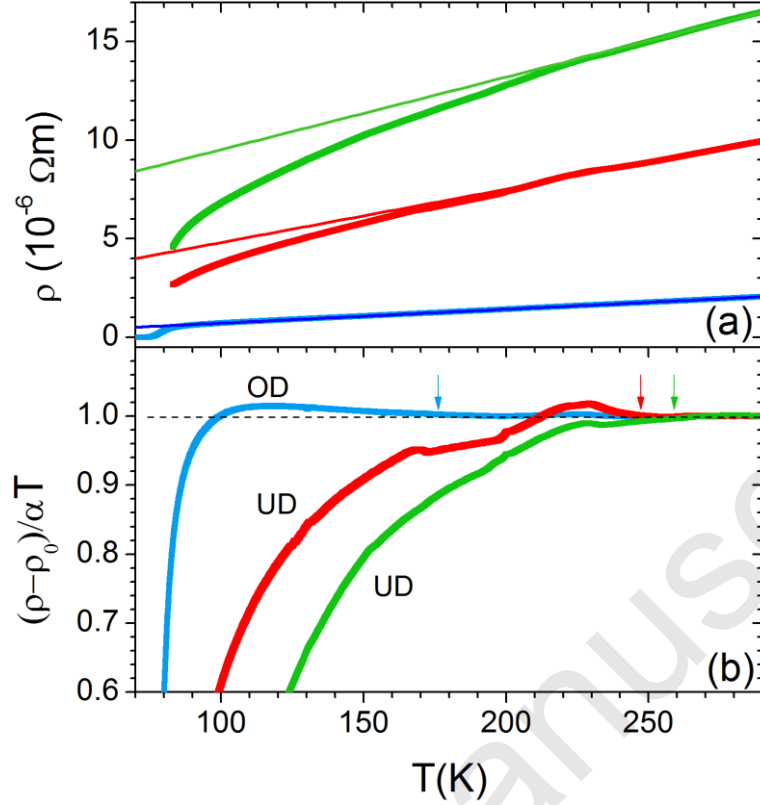


Figure 6. Panel (a): Temperature dependence of electrical resistivity ρ along with the straight lines corresponding to the extrapolation of their linear fit to the equation $\rho(T) = \rho_0 + \alpha T$ in the range 260-295 K. Blue lines refer to the sample before irradiation, red lines to the sample after a cumulative fluence $CF = 7.677 \times 10^{11} \text{ J/m}^2$ and a cumulated dose $CD = 3.909 \times 10^{12} \text{ Gy}$, and green lines after $CF = 15.354 \times 10^{11} \text{ J/m}^2$ and $CD = 7.816 \times 10^{12} \text{ Gy}$. Panel (b): Corresponding rescaled curves $(\rho(T) - \rho_0) / \alpha T$. Arrows indicate the temperature T^* at which the pseudogap opens. OD and UD refer to the overdoped and to the underdoped regime, respectively.

It is possible to see from Figure 6(a) that the resistivity at room temperature $\rho(RT)$ increases from about $2 \times 10^{-6} \text{ } \Omega\text{m}$ for the pristine material up to about $10 \times 10^{-6} \text{ } \Omega\text{m}$ after a cumulative fluence $CF = 7.677 \times 10^{11} \text{ J/m}^2$ and to $16.6 \times 10^{-6} \text{ } \Omega\text{m}$ after $CF = 15.354 \times 10^{11} \text{ J/m}^2$. The fact that X-ray irradiation has increased the material resistivity by a maximum factor of about 8 confirms that most of the resistance signal comes from unirradiated part of the sample, as previously hypothesized for the interpretation of Figure 5(b), therefore making our description of the system self-consistent. The monotonous increase of the resistivity with increasing the fluence shown in Figure 6(a) is in general agreement with what already observed for the radiation damage originated by both particles and photon sources^{18, 20, 27, 29-31}. More in details, it is possible to notice that the $\rho(RT)$ values obtained from our analysis lie approximately in the same range as the ones reported by Watanabe *et al.*³² and by Chen *et al.*²⁸ for Bi-2212 single crystals with different oxygen content δ induced by means of

equilibrium thermal treatments, but are lower by a factor of 2-3 with respect to the values corresponding to α -irradiated single crystals²⁷.

If compared to the results by Watanabe *et al.*³² following the procedure recently exploited by Torsello *et al.*¹⁹, the $\rho(T)$ values of Figure 6(a) would correspond to the non-stoichiometric oxygen contents $\delta=0.279$, $\delta=0.209$ and $\delta=0.199$ for the pristine, the $CF=7.677 \times 10^{11} \text{ J/m}^2$ and the $CF=15.354 \times 10^{11} \text{ J/m}^2$ curves, respectively. However, in the case of the irradiated material, these values certainly represent an underestimation of the real oxygen content δ because they ascribe all of the resistivity increase induced by irradiation only to the oxygen loss, neglecting the effect of grain boundaries. In this sense, these estimations have to be considered only as lower limits for δ of irradiated Bi-2212 in our experiment.

On the other hand, concerning the contribution of grain boundaries to the resistivity of the irradiated material, we can say that, from a qualitative point of view, our data seem not to support the *brick-wall* model for the current flow across grain boundaries of high temperature superconductors^{33, 34}, mainly because no contribution can be seen in the $\rho(T)$ curves from the *c*-axis resistivity, which should show a semiconducting behavior with a typical peak above T_c . Conversely, the *railway-switch* model^{35, 36} seems to be closer to our experimental situation, even if our observation of a substantial increase in resistivity and of the presence of [100]- and [010]-tilted grain boundaries indicates that some adjustment is necessary. In any case, detailed measurements of J_c and of its dependence on the magnetic field is required to tackle this problem on a quantitative level.

Figure 6(a) also shows the fit of the high temperature portion of the $\rho(T)$ curves to the linear relation $\rho(T)=\rho_0+\alpha T$. Indeed, it is well-known that in high-temperature superconductors the deviation from linearity of $\rho(T)$ depends on the doping level of the material³⁷⁻⁴¹. More specifically, the temperature where the $\rho(T)$ curve departs from linear behavior is considered a good estimation of T^* , i.e. of the temperature where the so-called pseudogap opens in the electronic DOS of the normal state⁴², as firstly observed both by ARPES⁴³ and STS⁴⁴ measurements. Figure 6(b) displays the same information in the form of the rescaled dimensionless behavior $\rho'=(\rho(T)-\rho_0)/\alpha T$ of the resistivity, according to the representation proposed by Ito *et al.*³⁷, where T^* corresponds to the departure from $\rho'=1$ and is indicated by the arrows. It is possible to observe that the pristine curve shows the typical behavior of OD materials, with a smooth upturn below $T^* \approx 172 \text{ K}$ before a steep decrease near T_c . On the contrary, the curve corresponding to $CF=7.677 \times 10^{11} \text{ J/m}^2$ shows a deviation from linearity at $T^* \approx 247 \text{ K}$, whereas the one corresponding to $CF=15.354 \times 10^{11} \text{ J/m}^2$ deviates at $T^* \approx 261 \text{ K}$. The general features of these latter two behaviors correspond to the gradual decrease of ρ' typical of UD materials, but a small oscillation is also noticeable on top of these curves just below T^* , whose origin is not clear. Nevertheless, the increase of T^* with the fluence confirms that X-ray irradiation has

promoted some shift of the material doping from the OD to the UD regime, in agreement with the indications coming from the length of the c -axis and from the qualitative estimation of δ .

Conclusions

In the present work we have investigated the mechanism of X-ray nanopatterning in a Bi-2212 single crystal via combined XRD and electrical resistance measurements. It has been shown that cumulative fluence values of the order of 10^{12} J/m² (corresponding to cumulative doses of the order of 10^{13} Gy) induce both oxygen loss from the material and an increase of crystal mosaicity, with the appearance of multiple nano-domains and corresponding grain boundaries. Both effects contribute in a synergistic way to change the superconducting and normal state electrical properties, which suggests the possibility of non-linear effects in these changes as a function of the cumulated fluence. This possibility could be very important to finely tune the structural defects as desired, and highlights how a careful assessment of the irradiation time is crucial to achieve a good control of X-ray nanopatterning. However, the understanding of its microscopic mechanisms is still far from being complete and further investigation is necessary.

Conflicts of interest

There are no conflicts to declare.

Acknowledgments

The authors thank the ESRF for the beamtime allocated and the ID13 beamline staff for their valuable help. They also gratefully acknowledge Compagnia di San Paolo for financial support to NanoFacility Piemonte at INRIM. This work has been partly carried out under project NANO-X jointly approved and funded by University of Torino and Compagnia di San Paolo. V.B. and M.T. acknowledge partial support from the “Departments of Excellence” (L. 232/2016) grant, funded by the Italian Ministry of Education, University and Research (MIUR).

References

1. H. M. Saavedra, T. J. Mullen, P. P. Zhang, D. C. Dewey, S. A. Claridge and P. S. Weiss, *Reports on Progress in Physics*, 2010, **73**, 036501.

2. B. Päiväntanta, A. Langner, E. Kirk, C. David and Y. Ekinici, *Nanotechnology*, 2011, **22**, 375302.
3. L. Malfatti, A. Pinna, S. Enzo, P. Falcaro, B. Marmiroli and P. Innocenzi, *J Synchrotron Radiat*, 2015, **22**, 165-171.
4. G. Agostini and C. Lamberti, *Characterization of semiconductor heterostructures and nanostructures*, Elsevier, 1 edn., 2008.
5. N. Poccia, M. Fratini, A. Ricci, G. Campi, L. Barba, A. Vittorini-Orgeas, G. Bianconi, G. Aeppli and A. Bianconi, *Nature Materials*, 2011, **10**, 733-736.
6. M. Truccato, A. Agostino, E. Borfecchia, L. Mino, E. Cara, A. Pagliero, N. Adhlakha, L. Pascale, L. Operti, E. Enrico, N. De Leo, M. Fretto, G. Martinez-Criado and C. Lamberti, *Nano Lett.*, 2016, **16**, 1669-1674.
7. W. Bras and H. Stanley, *Journal of Non-Crystalline Solids*, 2016, **451**, 153-160.
8. M. Truccato, G. Rinaudo, C. Manfredotti, A. Agostino, P. Benzi, P. Volpe, C. Paolini and P. Olivero, *Superconductor Science and Technology*, 2002, **15**, 1304.
9. M. Runde, J. L. Routbort, S. J. Rothman, K. C. Goretta, J. N. Mundy, X. Xu and J. E. Baker, *Phys. Rev. B*, 1992, **45**, 7375-7382.
10. M. M. R. Khan, S. Cagliero, A. Agostino, M. Beagum, C. Plapcianu and M. Truccato, *Supercond. Sci. Technol.*, 2009, **22**, 085011.
11. K. Inomata, T. Kawae, K. Nakajima, J. S. Kim and T. Yamashita, *Appl. Phys. Lett.*, 2003, **82**, 769-771.
12. J. C. Labiche, O. Mathon, S. Pascarelli, M. A. Newton, G. G. Ferre, C. Curfs, G. Vaughan, A. Homs and D. F. Carreiras, *Rev Sci Instrum*, 2007, **78**, 091301.
13. A. Le Bail, *Powder Diffraction*, 2005, **20**, 316-326.
14. J. Rodríguez-Carvajal, *Physica B: Condensed Matter*, 1993, **192**, 55-69.
15. A. P. Hammersley, S. O. Svensson, M. Hanfland, A. N. Fitch and D. Hausermann, *High Pressure Research*, 1996, **14**, 235-248.
16. B. L. Henke, E. M. Gullikson and J. C. Davis, *Atomic data and nuclear data tables*, 1993, **54**, 181-342.
17. H. Maeda, Y. Tanaka, M. Fukutomi and T. Asano, *Jpn. J. Appl. Phys.*, 1988, **27**, L209-L210.
18. A. Pagliero, L. Mino, E. Borfecchia, M. Truccato, A. Agostino, L. Pascale, E. Enrico, N. Leo, C. Lamberti and G. Martínez-Criado, *Nano Lett.*, 2014, **14**, 1583-1589.
19. D. Torsello, L. Mino, V. Bonino, A. Agostino, L. Operti, E. Borfecchia, E. Vittone, C. Lamberti and M. Truccato, *Phy Rev Mater*, 2018, **2**, 014801.
20. L. Mino, V. Bonino, A. Agostino, C. Prestipino, E. Borfecchia, C. Lamberti, L. Operti, M. Fretto, N. Leo and M. Truccato, *Scientific Reports*, 2017, **7**, 9066.
21. H. Hilgenkamp and J. Mannhart, *Reviews of Modern Physics*, 2002, **74**, 485-549.
22. D. Dimos, P. Chaudhari and J. Mannhart, *Phys. Rev. B*, 1990, **41**, 4038-4049.
23. Q. Li, Y. N. Tsay, Y. Zhu, M. Suenaga, G. D. Gu and N. Koshizuka, *Appl. Phys. Lett.*, 1997, **70**, 1164-1166.
24. J. Hanisch, A. Attenberger, B. Holzapfel and L. Schultz, *Phys. Rev. B*, 2002, **65**, 052507.
25. R. P. Gupta and M. Gupta, *Phys. Rev. Lett.*, 1996, **77**, 3216-3219.
26. S. K. Bandyopadhyay, P. Sen, P. Barat, U. De, K. Mandal, S. K. Kar and C. K. Majumdar, *Physica C: Superconductivity*, 1996, **267**, 303-307.
27. S. K. Bandyopadhyay, P. Barat, P. Sen, A. K. Ghosh, A. N. Basu and B. Ghosh, *Phys. Rev. B*, 1998, **58**, 15135-15145.
28. X. H. Chen, M. Yu, K. Q. Ruan, S. Y. Li, Z. Gui, G. C. Zhang and L. Z. Cao, *Phys. Rev. B*, 1998, **58**, 14219-14222.
29. F. Rullier-Albenque, A. Legris, H. Berger and L. Forro, *Physica C: Superconductivity*, 1995, **254**, 88-92.
30. G. Aldica, F. Vasiliu, I. I. Geru and B. M. Puscasu, *Journal of Superconductivity*, 2000, **13**, 623-631.

31. G. Aldica, S. Cagliero, A. Agostino, C. Lamberti and M. Truccato, *Supercond. Sci. Technol.*, 2011, **24**, 035009.
32. T. Watanabe, T. Fujii and A. Matsuda, *Phys. Rev. Lett.*, 1997, **79**, 2113-2116.
33. L. N. Bulaevskii, J. R. Clem, L. I. Glazman and A. P. Malozemoff, *Phys. Rev. B*, 1992, **45**, 2545-2548.
34. L. N. Bulaevskii, L. L. Daemen, M. P. Maley and J. Y. Coulter, *Phys. Rev. B*, 1993, **48**, 13798-13816.
35. B. Hensel, J. C. Grivel, A. Jeremie, A. Perin, A. Pollini and R. Flukiger, *Physica C: Superconductivity*, 1993, **205**, 329-337.
36. B. Hensel, G. Grasso and R. Flükiger, *Phys. Rev. B*, 1995, **51**, 15456-15473.
37. T. Ito, K. Takenaka and S. Uchida, *Phys. Rev. Lett.*, 1993, **70**, 3995-3998.
38. J. L. Tallon, J. W. Loram, G. V. M. Williams, J. R. Cooper, I. R. Fisher, J. D. Johnson, M. P. Staines and C. Bernhard, *Phys. Status Solidi B-Basic Res.*, 1999, **215**, 531-540.
39. B. Batlogg, H. Y. Hwang, H. Takagi, R. J. Cava, H. L. Kao and J. Kwo, *Physica C*, 1994, **235**, 130-133.
40. B. Wuyts, V. V. Moshchalkov and Y. Bruynseraede, *Phys. Rev. B*, 1996, **53**, 9418-9432.
41. H. Takagi, B. Batlogg, H. L. Kao, J. Kwo, R. J. Cava, J. J. Krajewski and W. F. Peck, *Phys. Rev. Lett.*, 1992, **69**, 2975-2978.
42. T. Timusk and B. Statt, *Reports on Progress in Physics*, 1999, **62**, 61-122.
43. H. Ding, T. Yokoya, J. C. Campuzano, T. Takahashi, M. Randeria, M. R. Norman, T. Mochiku, K. Kadowaki and J. Giapintzakis, *Nature*, 1996, **382**, 51-54.
44. C. Renner, B. Revaz, J. Y. Genoud, K. Kadowaki and O. Fischer, *Phys. Rev. Lett.*, 1998, **80**, 149-152.